PERGAMON

International Journal of Heat and Mass Transfer 43 (2000) 4043–4056

International Journal of HEAT and MASS TRANSFER

www.elsevier.com/locate/ijhmt

A first incursion into the 3D structure of natural convection of air in a differentially heated cubic cavity, from accurate numerical solutions

E. Tric*,[1], G. Labrosse, M. Betrouni[2]

Université Paris-Sud, CNRS-LIMSI, 91405 Orsay Cedex, France

Received 4 November 1998; received in revised form 12 November 1999

Abstract

Accurate solutions to the equations governing the natural convection of air in a cubic cavity, thermally driven on two vertically opposite faces, are given for Rayleigh number values up to 10^7. These solutions are obtained with a pseudo-spectral Chebyshev algorithm based on the projection–diffusion method [1,2] with a spatial resolution supplied by polynomial expansions, which go up to $111 \times 111 \times 111$. The solutions are believed to be accurate—better than (0.03, 0.05)% in relative global error for the corresponding Rayleigh number (Ra) range (10^3, 10^7). This clearly indicates a non monotonic evolution of the flow structure as Ra increases.

1. Introduction

A good knowledge of the natural convection of air in differentially heated enclosures is a valuable starting point for testing and validating computer codes used for a wide variety of practical problems, such as, cooling of radioactive waste containers, ventilation of rooms, solar energy collectors and crystal growth in liquids. The best reference, in this respect, must come from experiments that are specifically designed to supply benchmark data, which is not an easy task when dealing with adiabatic boundary conditions. A recent experimental contribution [3] must be taken note of, which concerns a cubic cavity even though the non-active (or side) walls are perfectly conducting. On the numerical side, in 1983, de Vahl Davis and Jones [4,5] published a benchmark solution of the buoyancy-driven flow in a square cavity with differentially heated vertical sides (the other ones being adiabatic) for a Rayleigh number (Ra) value lying in the range (10^3–10^6), and having a Prandlt number (Pr) fixed at 0.71. By resorting to a systematic grid refinement practice and concurrent use of the Richardson extrapolation to obtain grid-independent data, these solutions were claimed to be accurate to (0.1, 1)% in relative spatial error for Ra (10^4, 10^6). In 1991, Le Quéré [6] proposed accurate numerical solutions, obtained with a pseudo-spectral Chebyshev algorithm, for Ra values up to 10^8,

* Corresponding author.
E-mail address: tric@faille.unice.fr (E. Tric).
[1] Present address: Laboratoire Géosciences Azur, Université de Nice-Sophia Antipolis, 250 Av. A. Einstein, 06560 Valbonne, France.
[2] On leave from Institut de Physique, USTHB, El Alia, BP 32, Alger, Algeria.

0017-9310/00/$ - see front matter
PII: S0017-9310(00)00037-5

Nomenclature

d_{3D}	maximum nodal divergence in the cubic cavity, scaled by the largest modulus of the velocity
d_{2D}	maximum nodal divergence, in the square cavity scaled by the largest modulus of the velocity
d_{mp}	maximum of $(\partial v/\partial y)$ in the cavity mid-plane $(y = 0)$, scaled by the largest modulus of the velocity
$\hat{\mathbf{e}}_x$	unit vector in the horizontal direction
$\hat{\mathbf{e}}_y$	unit vector in the horizontal "depth" direction
$\hat{\mathbf{e}}_z$	unit vector in the upward vertical direction
Er	relative error
H	size of the square or cubic cavity
$\hat{\mathbf{n}}$	outward unit vector normal to the boundary domain $\partial\Omega$
N	number of nodes in each space direction.
Nu	Nusselt number
Pr	Prandlt number
p	dynamical pressure
Ra	Rayleigh number
T	temperature
t	time
u	velocity component along $\hat{\mathbf{e}}_x$
$\mathbf{v}$	velocity field
v	velocity component along $\hat{\mathbf{e}}_y$
w	velocity component along $\hat{\mathbf{e}}_z$
x	coordinate along $\hat{\mathbf{e}}_x$
y	coordinate along $\hat{\mathbf{e}}_y$
z	coordinate along $\hat{\mathbf{e}}_z$

Greek symbols

$\partial\Omega$	boundary of the closed domain
ΔT	temperature difference imposed between the two active vertical walls of the cavity
κ	thermal diffusivity
δt	time step
γ	acceleration field

Subscripts

mp	mid-plane
max	maximum of a quantity
2D	bidimensional case
3D	tridimensional case

which is very close to the transition into unsteadiness (at $Ra = (1.82 \pm 0.01) \times 10^8$, [7]).

In the last two decades, three-dimensional flow calculations have been performed for the differentially heated cavity (on two vertically opposite faces) using improved algorithms and computing resources [2,8–21]. All together, these papers refer to several different 3D configurations. In the one considered here, the fluid is confined in the three space directions and the non-active walls are adiabatic. To the authors' knowledge, only the references [2,10,12–14] supply characteristic values of the stationary velocity fields and/or the Nusselt numbers, for values of the Ra lying in the range $[10^3$–$10^7]$. It has been shown that the natural convection of air in such a configuration, becomes unsteady for a value of Ra situated just beyond this range, and exhibits hysteric behaviour for $Ra \in [3.2, 3.5] \times 10^7$ [2].

The purpose of this paper is to complete the two- and three-dimensional flow calculations database by providing five accurate solutions corresponding to $Ra = 10^3$, 10^4, 10^5, 10^6 and 10^7, respectively. These solutions come from a Chebyshev pseudo-spectral code. A comparison of our data with those already published is realised and a first set of "bench-mark three-dimensional solutions" is proposed. From a first glance at our results it can be deduced that the 3D flow structure does not evolve monotonically in this Ra range. The article is organized in sections which successively present the mathematical and numerical formulation of the natural convection flow, the validation and accuracy of our numerical 2D and 3D results, and the benchmark tridimensional solutions with some comments on the physics.

2. The Mathematical model and numerical method

Let ΔT be the imposed temperature difference between the two vertical active walls, and T_0 the mean temperature of the fluid. We are concerned here with the leading order in $\Delta T/T_0$ of the buoyant-induced flow in the cavity, knowing that there are possible departures of the second-order in experimental flows obtained at high values of the Rayleigh number. The usual dimensionless Boussinesq equations are then:

$$\frac{\partial \mathbf{v}}{\partial t} + (\mathbf{v}.\nabla)\mathbf{v} = -\nabla p + Pr\nabla^2\mathbf{v} + Ra\ Pr\ T\hat{\mathbf{e}}_z, \tag{1}$$

$$\nabla \cdot \mathbf{v} = 0, \tag{2}$$

$$\frac{\partial T}{\partial t} + (\mathbf{v} \cdot \nabla)T = \nabla^2 T, \tag{3}$$

where the lengths, the velocity $\mathbf{v}$, the temperature T are scaled by H, the size of cube, κ/H, the thermal diffusion velocity and ΔT, respectively. The other scales have been derived from these and Pr are fixed at 0.71.

The geometrical configuration is sketched in Fig. 1. No-slip boundary conditions are imposed on all the faces of the cube. The thermal conditions applied on the active faces are $T(x=\pm\frac{1}{2},\ y,\ z)=\mp\frac{1}{2}$, the other faces being adiabatic: $\frac{\partial T}{\partial \hat{n}}=0$, at $(x, y=\pm\frac{1}{2}, z)$ and $(x, y, z=\pm\frac{1}{2})$, where $\frac{\partial}{\partial \hat{n}}$ is the appropriate normal derivative. The 2D square configuration corresponds to the particular case of flows which are invariant by translation along the $\hat{\mathbf{e}}_y$ direction. It is often assumed that the approximate cross-section of the 3D flow is in the mid-plane $y=0$, which is invariant by reflection.

A Chebyshev Gauss–Lobatto method [22] has been used to evaluate the fields' spatial derivatives and the usual second-order Crank–Nicolson Adams–Bashforth finite difference scheme is called for time integration. The diffusion terms have been implicitly treated and the others ones explicitly. At each time step, the temperature is first updated to satisfy Eq. (3) and then one has to solve the resulting Stokes problem,

$$\begin{aligned}&\frac{\partial \mathbf{v}}{\partial t}+\nabla p-Pr\,\nabla^2\mathbf{v}=\mathbf{f}\equiv-(\mathbf{v}\cdot\nabla)\mathbf{v}+Ra\,Pr\,T\hat{\mathbf{e}}_z,\\ &\nabla\cdot\mathbf{v}=0,\end{aligned}\tag{4}$$

which can be equivalently written as ($f=0$ temporarily):

$$\nabla^2 p=0,\qquad \left(\frac{\partial}{\partial t}-Pr\nabla^2\right)\nabla^2\mathbf{v}=0.\tag{5}$$

It is well known that the numerical difficulty is to uncouple the velocity and pressure fields. For the 3D case, the cheapest approach in CPU time is to employ fractional step or splitting techniques. However, according to the analysis made in [23,24], this kind of method is not consistent with the Stokes problem (Eqs. (4) and (5)). Indeed, it amounts to get the set ($\mathbf{v}$, p) as solution of

$$\left(\alpha\frac{\partial}{\partial t}-\nabla^2\right)\nabla^2 p=0,$$

$$\left(\alpha\frac{\partial}{\partial t}-\nabla^2\right)\left(\frac{\partial}{\partial t}-Pr\,\nabla^2\right)\nabla^2\mathbf{v}=0,$$

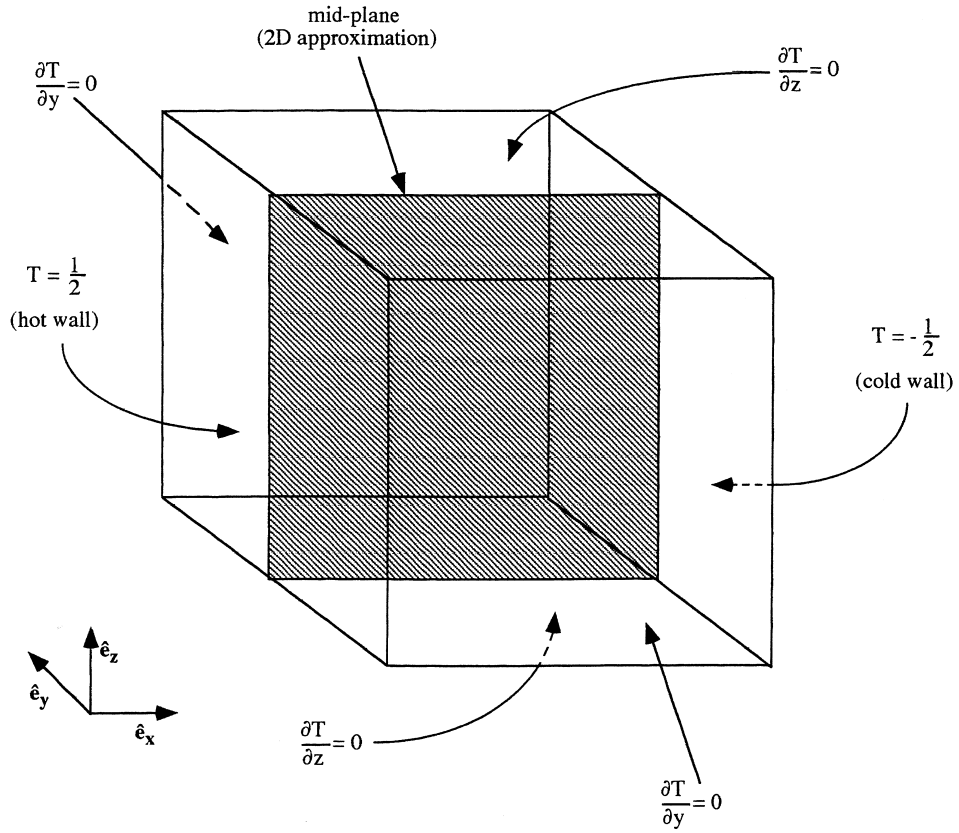

Fig. 1. Sketch of a physical model of the thermally driven cubic cavity.

Table 1
Comparison of our 2D air flow results with the bench-mark data proposed by de Vahl Davis [5] for $Ra = 10^3$, 10^4 and 10^5

	$Ra = 10^3$		$Ra = 10^4$		$Ra = 10^5$	
	Present work	Ref. [5]	Present work	Ref. [5]	Present work	Ref. [5]
Grid	51×51	Extrapolated	51×51	Extrapolated	51×51	Extrapolated
$u_{max}(0, z)$	3.66	3.65	16.18	16.18	34.70	34.73
z	0.313	0.313	0.323	0.323	0.354	0.355
$w_{max}(x, 0)$	3.71	3.70	19.63	19.62	68.61	68.59
x	−0.321	−0.322	−0.381	−0.382	−0.434	−0.434
$Nu_{2D,\,w}$	1.116	1.117	2.245	2.238	4.522	4.509
$Nu_{2D,\,0}$	1.116	1.118	2.245	2.243	4.522	4.519
Divergence	0.00826		0.00071		0.00082	

the constant α being related to time splitting. This splitting introduces an additional space-time operator on the physical fields, which is a modification of the Stokes problem in contradiction with the incompressibility hypothesis. As shown in [24], the projection–diffusion approach, recently proposed in [1,2], is consistent with Eq. (5) and therefore recommended for correctly capturing the threshold of the onset of unsteadiness [2]. This latter method presents the same CPU cost and has been chosen for this study. Its main features are: unconditional stability [24] with the second-order temporal schemes and it proceeds in two steps. First, the pressure and an acceleration field, γ, are evaluated from the Darcy system,

$$\gamma + \nabla p = \mathbf{f}$$

$$\gamma \cdot \hat{\mathbf{n}}|_{\partial\Omega} = Pr(\nabla \times \nabla \times v) \cdot \hat{\mathbf{n}}|_{\partial\Omega},$$

$$\nabla \cdot \gamma = 0,$$

where $(\nabla \times \nabla \times \mathbf{v}).\hat{\mathbf{n}}|_{\partial\Omega}$ is explicitly evaluated with time. To apply the incompressibility constraint $\nabla \cdot \gamma = 0$, on the boundaries, this boundary condition is taken into account, instead of the corresponding component of the first equation. This field is *exactly solenoïdal*, and is in turn, the source of the diffusion step,

$$\left(\frac{\partial}{\partial t} - Pr \cdot \nabla^2\right)\mathbf{v} = \gamma,$$

$$\mathbf{v}|_{\partial\Omega} = 0, \tag{6}$$

and is easily solved by a standard successive diagonalization technique [25,26]. This latter stage is a classical (vectorial) heat equation problem. The numerical convergence, with the nodes number of its solution, has been analysed at the very beginning of the intensive use of the spectral methods [22,27]. It is well known that the leading part of the numerical error comes from the truncation on the right-hand side of Eq. (6), a truncation coming from taking the boundary conditions into account. Hence, γ is exactly solenoïdal, but it is truncated for solving Eq. (6), and the resulting solution $\mathbf{v}$ cannot be divergence free. Moreover, assuming that the expected solution is regular, references [22] and [27] tell us that the truncation, vanishes exponen-

Table 2
Comparison of our 2D air flow results with the bench-mark data proposed by Le Quéré [6] for $Ra = 10^6$, 10^7 and 10^8

	$Ra = 10^6$		$Ra = 10^7$		$Ra = 10^8$	
	Present work	Ref. [6]	Present work	Ref. [6]	Present work	Ref. [6]
Grid	51×51	73×73	51×51	81×81	129×129	129×129
$u_{max}(0, z)$	64.84	64.83	148.60	148.59	321.87	321.90
z	0.341	0.342	0.379	0.379	0.428	0.428
$w_{max}(x, 0)$	220.50	220.60	700.10	699.18	2222.38	2222.39
x	−0.462	−0.462	−0.479	−0.479	−0.488	−0.488
$Nu_{2D,\,w}$	8.825	8.825	16.522	16.523	30.225	30.225
$Nu_{2D,\,0}$	8.825	8.825	16.522	16.523	30.225	30.225
Divergence	0.0123	7×10^{-9}	0.0833	1.2×10^{-8}	0.0192	5×10^{-8}

tially with the nodes number and so does the resulting $\nabla \cdot \mathbf{v}$ field. This means that the obtained numerical solution is the closest one can get to the physical one.

There is another way of admitting why the best numerical solution is not a priori divergence free. Let us assume that the analytical solution is known. Then, the field $\mathbf{v}_N$ of its collocated values, on a N^3 grid is exact, but has a non-zero numerical divergence, d_N, which vanishes asymptotically with N. If, by some numerical method, its divergence is forced to cancel, the nodal values of the new field $\mathbf{v}'_N$, will unavoidably depart from their exact values, by an amount of the order of $\|\delta \mathbf{v}_N\| \leq \|d_N\|/N^2$, $\|\cdot\|$ stands for the order of magnitude of the enclosed term. This will be later on called for, to estimate the compatibility between numerical velocity fields obtained with different $\nabla \cdot \mathbf{v}$ treatments. The effective convergence to zero of $\nabla \cdot \mathbf{v}$, with the mesh refinement, is actually the best indication of the spectral quality of the numerical velocity field. Nonetheless, there is no a priori estimate of the acceptable value of $\nabla \cdot \mathbf{v}$ which ensures a given accuracy of the solution. Of course, the exponential decrease is expected to saturate at some level because of rounding-off errors. The convergence of results of the "projection–diffusion" solver, with the meshing, has been measured with various situations of confined fluid flows. These results compare quite well with those obtained from a different uncoupling approach, of the Uzawa type. Reference [2] reports such a comparison for the thermally driven 2D cavity. For both Stokes solvers, the effective convergence of the numerical $\nabla \cdot \mathbf{v}$ field to zero is non-monotonic, but bound by an exponentially decreasing envelop, as the nodes, number increases. A similar behaviour is reported here.

3. The numerical results

Convergence to steadiness is declared when the criterion,

$$\frac{|\phi_n - \phi_{n-1}|}{|\phi_n|} \leq 10^{-1} \cdot \delta t$$

is satisfied for all ϕ, ϕ_n standing for the maximum absolute value, found on the nodes at time $n\delta t$, for one of the physical fields (the velocity components or temperature). A more severe criterion, up to 10^{-4} instead of 10^{-1}, has been taken to obtain 3D results at $Ra = 10^6$, with $\delta t = 4 \times 10^{-6}$ and a meshing of 81^3. The numerical results depart by 0.03% from those

Table 3
Characteristic values, $Ra = 10^3$

Grid	51^3	61^3	71^3	81^3
$u_{\max}$	3.54356	3.54351	3.54353	3.54356
x	0.0166	0.0165	0.0166	0.0166
y	0.56×10^{-10}	0.74×10^{-11}	0.95×10^{-11}	0.54×10^{-11}
z	0.3169	0.3169	0.3169	0.3169
$v_{\max}$	0.17332	0.17331	0.17331	0.17331
x	0.14×10^{-10}	0.14×10^{-10}	0.14×10^{-10}	0.14×10^{-10}
y	0.2521	0.2521	0.2521	0.2521
z	0.44×10^{-10}	0.44×10^{-10}	0.44×10^{-10}	0.43×10^{-10}
$w_{\max}$	3.54477	3.54482	3.54467	3.54469
x	0.3233	0.3223	0.3223	0.3223
y	0.24×10^{-10}	0.21×10^{-10}	0.19×10^{-10}	0.38×10^{-10}
z	0.32×10^{-2}	0.32×10^{-2}	0.32×10^{-2}	0.32×10^{-2}
$U_{\text{mp, max}}$	3.54356	3.54351	3.54353	3.54356
x	0.0166	0.0166	0.0166	0.0166
z	0.3169	0.3169	0.3169	0.3169
$W_{\text{mp, max}}$	3.54477	3.54482	3.54467	3.54477
x	0.3233	0.3233	0.3233	0.3233
z	0.32×10^{-2}	0.32×10^{-2}	0.32×10^{-2}	0.32×10^{-2}
$U_{\text{mp, max}}(0, 0, z)$	3.53621	3.53873	3.53878	3.53875
z	0.3192	0.3151	0.3151	0.3151
$W_{\text{mp, max}}(x, 0, 0)$	3.54311	3.54162	3.54186	3.54185
x	−0.3187	−0.3147	−0.3147	−0.3147
Nu_{mp}	1.0874	1.0873	1.0873	1.0873
$Nu_{\text{3D, W}}$	1.0700	1.0700	1.0700	1.0700
d_{3D}	0.263×10^{-3}	0.222×10^{-3}	0.978×10^{-4}	0.103×10^{-4}
d_{mp}	0.286	0.286	0.286	0.286

Table 4
Characteristic values, $Ra = 10^4$

Grid	51^3	61^3	71^3	81^3
u_{max}	16.71828	16.72060	16.71955	16.71986
x	0.0196	0.0196	0.0196	0.0196
y	0.323×10^{-10}	0.731×10^{-10}	0.181×10^{-10}	0.120×10^{-10}
z	0.3250	0.3250	0.3250	0.3250
v_{max}	2.15622	2.15767	2.15661	2.15657
x	0.3823	0.3823	0.3823	0.3823
y	0.2826	0.2826	0.2826	0.2826
z	0.3447	0.3447	0.3447	0.3447
W_{max}	18.98182	18.98266	18.98359	18.98359
x	0.2308	0.2308	0.2308	0.2308
z	0.0206	0.0206	0.0206	0.0206
$u_{mp,\ max}$	16.71828	16.72060	16.71965	16.71986
x	0.0196	0.0196	0.0196	0.0196
z	0.3250	0.3250	0.3250	0.3250
$W_{mp,\ max}$	18.68140	18.68290	18.68266	18.68247
x	0.3870	0.3870	0.3870	0.3870
z	0.0219	0.0219	0.0219	0.0219
$u_{mp,\ max}(0, 0, z)$	16.70562	16.66930	16.72155	16.72128
z	0.3185	0.3346	0.3248	0.3244
$W_{mp,\ max}(x, 0, 0)$	18.62812	18.61046	18.61681	18.61615
x	−0.3853	−0.3886	−0.3809	−0.3802
N_{mp}	2.2505	0.2505	2.2505	2.2505
$N_{3D,\ w}$	2.0542	2.0542	2.0542	2.0542
d_{3D}	0.718×10^{-3}	0.524×10^{-3}	0.490×10^{-3}	0.280×10^{-3}
d_{mp}	0.541	0.541	0.541	0.541

obtained with the criterion 10^{-1}. This error has been added to the one due to the spatial resolution (see below).

All the maxima that will be presented for the velocity components have been obtained by using a second-order Lagrangian interpolation, between three adjacent nodal values in each space direction. In contrast, for the velocity divergence (scaled by the largest modulus of the velocity), the maxima comes merely from the nodal values of this field. Owing to the centro- and reflection symmetry properties of these flows [2], the locations of all the quoted maxima have been restricted to the ($y \geq 0$, $z \geq 0$) sub-domain of the cavity.

The dimensionless heat transfer rates at the cold isothermal wall are represented by the Nusselt numbers, defined as follows.

(a) The 3D local Nusselt $Nu_{local}(x, z) = \frac{\partial T(y, z)}{\partial x}|_{x=1/2}$
(b) The vertically averaged Nusselt $Nu(y) = \int_{-1/2}^{1/2} Nu_{local}(y, z)\, dz$
(c) The global 3D Nusselt number at the wall $Nu_{3D,\ w} = \int_{-1/2}^{1/2} Nu(y)\, dy$
(d) The mid-plane Nusselt number $Nu_{mp} = Nu(y = 0)$.
(e) The global 2D Nusselt number at the wall is $Nu_{2D,\ w} = \int_{-1/2}^{1/2} \frac{\partial T(z)}{\partial x}|_{x=1/2}\, dz$
(f) The global 2D Nusselt number at $x = 0$, $Nu_{2D},\ 0 = \int_{-1/2}^{1/2} \frac{\partial T(z)}{\partial x}|_{x=0}\, dz$.

The derivations and integrations have been spectrally computed.

2D and 3D calculations have been performed for each chosen Ra, applying the following procedure. For a given value of Ra, a steady solution has been first obtained on a coarser grid, starting either from rest or from flow corresponding to a smaller Ra. This solution was then projected onto a finer Gauss–Lobatto grid by a Lagrangian interpolant. Time integration was then restarted, using this extrapolated flow as initial condition, and carried out until the new steady-state was achieved. The process was repeated until the solution was obtained on the finest grid.

All the 2D flows mentioned in this subsection have been obtained with a 51^2 grid and $\delta t = 4 \times 10^{-5}$, except for $Ra = 10^8$ for which the grid has been refined up to 129^2 ($\delta t = 4 \times 10^{-6}$). Systematic comparisons have been made for the 2D case, with the benchmark data proposed by [5,6], for $Ra = 10^3$–10^5 and $Ra = 10^6$–10^8, respectively. These data and ours are gathered in Tables 1 and 2, where the maxima (on the square cavity) and their location of (a) the horizon-

tal velocity component at $x = 0$, (b) the vertical velocity component, at $z = 0$ and (c) the Nusselt numbers $Nu_{2D,\,0}$ and $Nu_{2D,\,W}$ are presented. An excellent agreement is observed between the sets of data, except for the numerical values of $\nabla \cdot \mathbf{v}$ with respect to the data from [6]. This is clearly due to the different choices made for uncoupling the velocity and pressure fields in the Stokes stage. In [6], the velocity field is forced to be exactly solenoïdal. This allows to confirm the comments made in Section 2. In particular, the expected order of magnitude of the relative difference between the two quoted values for $w_{\max}(x, 0)$ is $\frac{\|\delta v_N\|}{\|v_N\|} \leq \frac{\|d_N\|}{\|v_N\|} \cdot \frac{1}{N^2}$. Since the divergence quoted in the tables of this paper is $\|d_N\|/\|\mathbf{v}_N\|$, it is easy to estimate the compatibility between the present results and those of [6]. The maximum one can expect for the order of the magnitude of $\|\delta \mathbf{v}_N\|$, with grid 129^2, is thus 0.035, in good agreement with $\|\delta \mathbf{v}_N\| \approx 0.01$ coming from Table 2. Having in mind the computational cost of the 3D flows, and the extremely expensive methods (Uzawa or influence matrix) to get an exactly satisfied $\nabla \cdot \mathbf{v} = 0$ constraint, one can point out the great advantage that a method, such as the "projection-diffusion", which offers to supply spectrally accurate flows, at the price of four direct Helmholtz solvers [23,24].

3D calculations have been performed at five Rayleigh number values (10^3, 10^4, 10^5, 10^6 and 10^7) of which the respective results are reported in Tables 3–7. For each of these values, a 3D flow has been obtained with four different meshings (51^3, 61^3, 71^3 and 81^3). The particular case of $Ra = 10^7$ has been computed with a meshing going up to 111^3. To characterise the spatial convergence of these different steady flows, each table contains the following quantities: (a) the maximum of each velocity component in the cavity, with its location; (b) the maximum of the u and w components ($\mathbf{v}$ cancels there) in the mid-plane ($y = 0$), with their locations; (c) the maximum of the u component at $x = 0$ and w component at $z = 0$ in the mid-plane ($y = 0$), and their locations; (d) the Nusselt numbers $Nu_{3D,\,W}$ and Nu_{mp}; and (e) d_{3D}, d_{mp}. All these tables show that the position of the quoted velocity extrema are accurately determined for all the chosen grids. The numerical values of the velocity components and of d_{3D} present a good convergence, which is assessed below.

The $Ra = 10^6$ and 10^7 flows have indeed been obtained with other intermediate grids, in order to get a clean measurement of the convergence rates of the data with the number of nodes. Table 8 refers to the

Table 5
Characteristic values, $Ra = 10^5$

Grid	51^3	61^3	71^3	81^3
$u_{\max}$	43.9089	43.9039	43.9012	43.9037
x	−0.1841	−0.1841	−0.1841	−0.1841
y	0.2203	0.2203	0.2203	0.2203
z	0.3873	0.3873	0.3873	0.3873
$v_{\max}$	9.7004	9.6998	9.6970	9.6973
x	0.4175	0.4175	0.4175	0.4175
y	0.3390	0.3390	0.3390	0.3390
z	0.3801	0.3801	0.3801	0.3801
$W_{\max}$	71.1053	71.0611	71.0599	71.0680
x	0.4305	0.4304	0.4304	0.4304
y	0.3736	0.3736	0.3736	0.3736
z	0.623×10^{-2}	0.603×10^{-2}	0.604×10^{-2}	0.604×10^{-2}
$u_{mp,\,max}$	43.0630	43.0673	43.0549	43.0610
x	−0.1864	−0.1865	−0.1865	−0.1865
z	0.3848	0.3848	0.3848	0.3848
$W_{mp,\,max}$	65.4395	65.4404	65.4313	65.4362
x	0.4368	0.4368	0.4368	0.4368
z	0.0100	0.0100	0.0100	0.0100
$u_{mp,\,max}(0, 0, z)$	37.3998	37.5545	37.5683	37.5612
z	0.3425	0.3535	0.3535	0.3535
$W_{mp,\,max}(x, 0, 0)$	65.3572	65.3105	65.2157	65.2113
x	−0.4382	−0.4330	−0.4330	−0.4330
N_{mp}	4.6133	4.6131	4.6127	4.6127
$N_{3D,\,W}$	4.3375	4.3373	4.3371	4.3370
d_{3D}	0.390×10^{-2}	0.196×10^{-2}	0.130×10^{-2}	0.112×10^{-2}
d_{mp}	0.421	0.421	0.421	0.421

Table 6
Characteristic values, $Ra = 10^6$

Grid	51^3	61^3	71^3	81^3
u_{max}	126.9468	127.0183	126.9724	126.9731
x	−0.3057	−0.3057	−0.3057	−0.3057
y	0.2996	0.2997	0.2997	0.2997
z	0.4369	0.4365	0.4365	0.4365
v_{max}	25.5664	025.5664	25.5675	25.5650
x	0.4518	0.4518	0.4518	0.4518
y	0.3983	0.3983	0.3983	0.3983
z	0.4168	0.4169	0.4168	0.4168
W_{max}	236.7254	236.7222	236.7255	236.7203
x	0.4603	0.4604	0.4604	0.4604
y	0.4301	0.4299	0.4299	0.4299
z	0.0265	0.0266	0.0265	0.0265
$u_{mp,\ max}$	123.483	123.4956	123.4750	123.4777
x	−0.3133	−0.3133	−0.3133	−0.3133
z	0.4366	0.4366	0.4366	0.4366
$W_{mp,\ max}$	218.2468	218.2018	218.2506	218.2578
x	0.4638	0.4638	0.4638	0.4638
z	0.0353	0.0353	0.0353	0.0353
$u_{mp,\ max}(0, 0, z)$	67.9673	68.2109	68.2162	68.2198
z	0.3645	0.3535	0.3634	0.3536
$W_{mp,\ max}(x, 0, 0)$	216.9556	216.5737	216.5739	217.5702
x	−0.4649	−0.4668	−0.4669	−0.4669
N_{mp}	8.8772	8.8771	8.8771	8.8771
$N_{3D,\ w}$	8.6408	8.6407	8.6407	8.6407
d_{3D}	0.0248	0.0123	0.0654×10^{-2}	0.363×10^{-2}
d_{mp}	0.130	0.130	0.130	0.130

10^7 case only, to show how the maxima of the velocity components and d_{3D} converge with the grid refinement. As the number of nodes increase, each quantity converges towards a given value (zero, in particular, for the divergence). The exponential decrease of the relative divergence, as a function of N^3, shown in Fig. 2a and b, for $Ra = 10^6$ and 10^7, respectively, is not quite monotonic but nevertheless confirms the spectral improvement of the data. In order to estimate this improvement and the error associated with the spatial resolution, for each maxima of the velocity components given in Table 8, as well as for the $Ra = 10^6$ case, we have calculated the quantity

$$Er\left(\phi^{N_1}\right) = \frac{|\phi^{N_1}_{max} - \phi^{N_1}_{max}|}{|\phi^{N_1}_{max}|}, \quad N_2 = N_1 + 6 \text{ (or 4 alternatively)}$$

where $\phi^{N_i}_{max}$ stands for the absolute maximum of one of the velocity components, obtained with the N_i^3 grid. Here also, the evolution of these relative errors (Fig. 2a and b) as a function of N^3 is non-monotonic, but bounded by a decreasing exponential-like envelope. Among the many reasons which can be invoked to interpret the observed fluctuations, one is the amplification of the divergence fluctuation by an $O(N^2)$ coefficient (see Section 2), the non-regular meshing in N of Er, and the overlapping of the successive grid nodes around the maximum. A given number of significant digits emerges from this behaviour on which the forthcoming bench mark data are based. Moreover, with the finest grid used here (81^3 and 111^3 nodes for $Ra = 10^6$ and 10^7, respectively), the relative accuracy is within 0.02%. Repeating this procedure at $Ra = 10^3$ and 10^4 with the four meshings indicated in Tables 3 and 4, the corresponding relative error is evaluated at 0.002%. These data can then be considered as worthy of being communicated as the previously published 2D bench mark data, and as a contribution to the numerical attempts for obtaining accurate 3D flows.

4. Benchmark solutions

From all the previously presented data, the subset which corresponds to the 3D "benchmark solutions" is gathered in Table 9, for Ra values lying in the range

Table 7
Characteristic values, $Ra = 10^7$

Grid	51^3	61^3	71^3	81^3	91^3	101^3	111^3
u_{max}	383.9579	383.1580	383.7974	383.7851	383.8998	383.8474	383.8357
x	−0.3777	−0.3777	−0.3777	−0.3777	−0.3777	−0.3777	−0.3777
y	0.16×10^{-9}	0.36×10^{-10}	0.36×10^{-10}	0.37×10^{-10}	0.37×10^{-10}	0.37×10^{-10}	0.37×10^{-10}
z	0.4663	0.4663	0.4663	0.4663	0.4663	0.4663	0.4663
v_{max}	83.4998	83.3978	83.3878	83.4011	83.3883	83.3880	83.3885
x	−0.3316	−0.3311	−0.3311	−0.3311	−0.3311	−0.3311	−0.3311
y	0.4078	0.4083	0.4083	0.4083	0.4083	0.4083	0.4083
z	0.3953	0.3955	0.3955	0.3955	0.3955	0.3955	0.3955
W_{max}	767.2357	768.2554	768.1611	768.0697	768.2578	768.1588	768.1393
x	0.4775	0.4775	0.4775	0.4775	0.4775	0.4775	0.4775
y	0.4599	0.4601	0.4601	0.4601	0.4601	0.4601	0.4601
z	0.0323	0.0323	0.0323	0.0323	0.0323	0.0323	0.0323
$u_{mp,\ max}$	383.9578	383.8139	383.7974	383.7650	383.8502	383.8474	383.8358
x	−0.3777	−0.3777	−0.3777	−0.3777	−0.3777	−0.3777	−0.3777
z	0.4663	0.4662	0.4662	0.4662	0.4662	0.4662	0.4662
$W_{mp,\ max}$	699.9631	699.9619	698.1931	698.4449	698.5730	698.5115	698.5260
x	0.4794	0.4794	0.4794	0.4794	0.4794	0.4794	0.4794
z	0.354×10^{-1}	0.354×10^{-1}	0.354×10^{-1}	0.354×10^{-1}	0.354×10^{-1}	0.354×10^{-1}	0.354×10^{-1}
$u_{mp,\ max}(0, 0, z)$	153.5326	154.6107	154.8579	154.5689	154.6098	154.9197	154.9035
z	0.3853	0.3716	0.3716	0.3716	0.3716	0.3716	0.3716
$W_{mp,\ max}(x, 0, 0)$	686.5947	686.5947	686.5951	689.9350	692.8499	692.6914	692.6296
x	−0.4755	−0.4755	−0.4755	−0.4812	−0.4806	−0.4806	−0.4806
N_{mp}	16.5471	16.5477	16.5477	16.5477	16.5477	16.5477	16.5477
$N_{3D,\ w}$	16.3422	16.3427	16.3427	16.3427	16.3427	16.3427	16.3427
d_{3D}	0.160	0.101	0.057	0.032	0.015	0.0103	0.0069
d_{mp}	0.207	0.206	0.207	0.206	0.206	0.206	0.206

(10^3, 10^7). The quoted data are purposely restricted to their significant digits. As already indicated in [2], all these flows are invariant by reflection about the mid-plane ($y = 0$). The measured relative symmetry rate is better than 10^{-9}. For the sake of comparison, we have collected the available published 3D results with ours in Tables 10–13. In spite of the large variety of the chosen numerical methods and meshings, these data compare quite satisfactorily.

The goal of this paper is not to characterise the 3D structure of the flows. Nonetheless, a noticeable feature emerges from Table 9. Indeed, the mid-plane contains the maxima of the velocity component u, except for the $Ra = 10^5$ and 10^6 cases, which suggests a non-monotonic evolution of the flow structure as the Ra number increases. This is confirmed by looking at the three relative heat transfer rates, $100 \times (Nu_{2D,\ W}, -Nu_{3D,\ W},)/Nu_{2D,\ W}$, $100 \times (Nu_{2D,\ W}, -Nu_{mp})/Nu_{2D,\ W}$, and $100 \times (Nu_{3D,\ W}, -Nu_{mp})/Nu_{3D,\ W}$, whose Ra dependencies are shown in Fig. 3. It is well known since the thermally driven 3D cavity was first studied, $Nu_{3D,\ W}$ is less than $Nu_{2D,\ W}$, at least until the onset of unsteadiness, their relative departure being maximum (9%) at about $Ra = 10^4$. With respect to

Table 8
Maxima of the velocity components and the divergence, with different grids. 3D air flows, $Ra = 10^7$

Grid	u_{max}	v_{max}	w_{max}	d_{3D}
21^3	377.2774	77.2720	777.4633	1.18
27^3	384.1558	83.2424	745.9628	0.749
31^3	384.7545	83.5144	767.9119	0.465
37^3	384.6206	83.6662	765.0922	0.388
41^3	384.2962	83.5652	768.1678	0.290
47^3	383.3162	83.4702	766.4531	0.210
51^3	383.9579	83.4998	767.2357	0.160
57^3	383.2419	83.3944	767.3424	0.126
61^3	383.1580	83.3978	768.2254	0.101
67^3	383.8643	83.3926	768.5642	0.072
71^3	383.7974	83.3878	768.1611	0.057
77^3	383.7872	83.4039	768.0607	0.041
81^3	383.7851	83.4011	768.0697	0.032
87^3	383.8072	83.3887	767.9471	0.019
91^3	383.8998	83.3883	768.2578	0.015
97^3	383.7989	83.3888	767.9627	0.012
101^3	383.8474	83.3880	768.1588	0.103
107^3	383.8167	83.3882	768.1035	0.0081
111^3	383.8357	83.3885	768.1393	0.0069

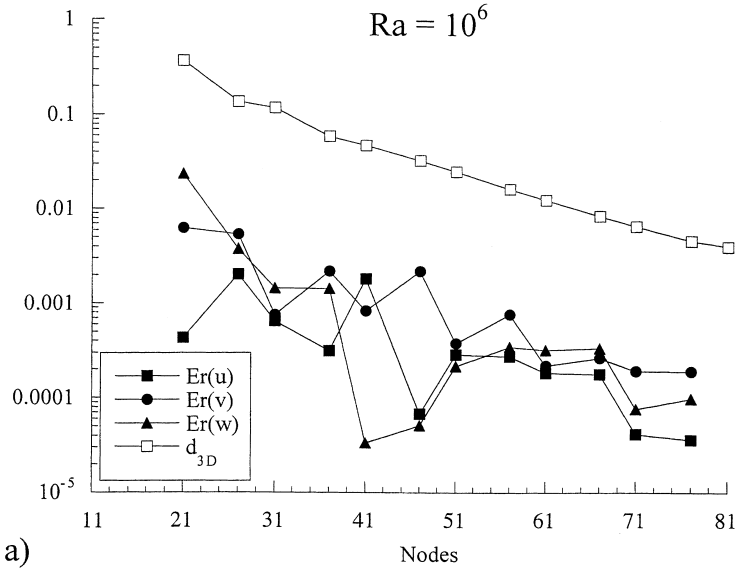

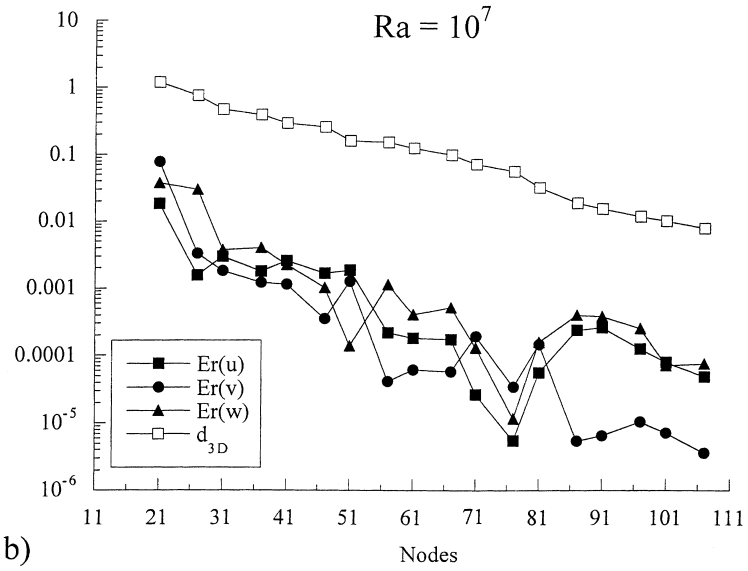

Fig. 2. The maximum (pointwise) velocity divergence, and the relative error (defined in the text) in each maximum of the velocity component, as a function of the number of nodes in each spatial direction.

$Nu_{2D,\,W}$, the mid-plane heat transfer increases, reaching a maximum (at about $Ra = 10^5$) and then goes back to get close to, but slightly larger than, $Nu_{2D,\,W}$. So, the 2D approximation of the natural convection of air overestimates the effective 3D heat transfer and surprisingly, underestimates the mid-plane effective heat transfer rate. While $Nu_{2D,\,W}$ gives the worst estimation of $Nu_{3D,\,W}$, it is the best for Nu_{mp}. With respect to Nu_{mp}, the 3D heat transfer is always weaker. The minimum it presents (by almost 10% at about $Ra = 10^4$) indicates a strong y-dependency of $Nu(y)$. The last data, at $Ra = 3.3 \times 10^7$, comes from the ultimate steady flow obtained before the onset of unsteadiness reported in reference [2]. It has been added to the Benchmark data in Fig. 3 in order to clarify the heat transfer rate evolution at the boundary of the steady

Table 9
Benchmark solutions

	$Ra = 10^3$	$Ra = 10^4$	$Ra = 10^5$	$Ra = 10^6$	$Ra = 10^7$
u_{max}	3.543	16.719	43.90	126.97	383.8
x	0.0166	0.0196	−0.1841	−0.3057	−0.3777
y	0.54×10^{-11}	0.12×10^{-10}	0.2203	0.2997	0.37×10^{-10}
z	0.3169	0.3250	0.3873	0.4365	0.4663
v_{max}	0.173	2.156	9.69	25.56	83.38
x	0.14×10^{-10}	0.3823	0.4175	0.4518	−0.3311
y	0.2521	0.2826	0.3390	0.3983	0.4083
z	0.43×10^{-10}	0.3447	0.3801	0.4168	0.3955
W_{max}	3.544	18.983	71.06	236.72	768.1
x	0.3223	0.3834	0.4304	0.4604	0.4775
y	0.38×10^{-10}	0.2308	0.3736	0.4299	0.4601
z	0.0032	0.0206	0.0060	0.0265	0.0323
$u_{mp,\ max}$	3.543	16.719	43.06	123.47	383.8
x	0.0166	0.0196	−0.1865	−0.3133	−0.3777
z	0.3169	0.3250	0.3848	0.4366	0.4662
$W_{mp,\ max}$	3.544	18.682	65.43	218.25	698.5
x	0.3233	0.3870	0.4368	0.4638	0.4794
z	0.0032	0.0219	0.0100	0.0353	0.0354
$u_{mp,\ max}(0, 0, z)$	3.538	16.721	37.56	68.21	154.9
z	0.3151	0.3244	0.3535	0.3536	0.3716
$W_{mp,\ max}(x, 0, 0)$	3.541	18.616	65.21	217.57	692.6
x	−0.3147	−0.3802	−0.4330	−0.4669	−0.4806
N_{mp}	1.087	2.250	4.612	8.877	16.547
$N_{3D,\ w}$	1.070	2.054	4.337	8.640	16.342
d_{3D}	0.103×10^{-4}	0.280×10^{-3}	0.112×10^{-2}	0.363×10^{-2}	0.0069
d_{mp}	0.286	0.541	0.421	0.130	0.206

flows domain. Unsteadiness occurs before the 2D and 3D heat transfer rates get too close. The 3D structure of these flows therefore, deserves to be studied in detail.

5. Conclusion

Accurate solutions to the differentially heated cubic cavity problem have been presented, for values of Ra in the range $(10^3, 10^7)$, that is almost up to the end of the steady laminar regime. From mesh refinements and extrapolations, the spatial resolution of the data is believed to be better than 0.02% in relative spatial error at the highest Rayleigh number. A non-monotonous dependency on the Rayleigh number of the flow structure emerges clearly from the quoted benchmark data.

Table 10
Compared $Ra = 10^3$ air flow results

	$Ra = 10^3$		$Ra = 10^4$	
Grid	Ref. [13] 32^3	Present work 81^3	Ref. [13] 32^3	Present work 81^3
$u_{mp,\ max}(0, 0, z)$	3.5012	3.538	16.962	16.721
z	0.3	0.3151	0.3167	0.3244
$W_{mp,\ max}(x, 0, 0)$	3.5172	3.541	18.976	18.616
x	−0.3333	−0.3147	−0.3833	−0.3802
N_{mp}	1.105	1.087	2.302	2.250
$N_{3D,\ w}$	1.085	1.070	2.100	2.054

Table 11
Compared $Ra = 10^5$ 3D air flow results

	$Ra = 10^5$			
Grid	Ref. [13] 62^3	Ref. [15] 27^3	Ref. [9] 25^3	Present work 81^3
u_{max}		43.75		43.90
x		−0.171		−0.1841
y		0.208		0.2203
z		0.382		0.3873
v_{max}		9.65	9.2	9.69
x		0.412		0.4175
y		0.332		0.3390
z		0.374		0.3801
W_{max}		71.47	70.4	71.06
x		0.432		0.4304
y		0.372		0.3736
z		0.03		0.604×10^{-2}
$u_{mp,\ max}(0, 0, z)$	39.116			37.56
z	0.3547			0.3535
$W_{mp,\ max}(x, 0, 0)$	65.841			65.21
x	−0.4353			−0.4330
N_{mp}	4.646	4.613		4.612
$N_{3D,\ W}$	4.361	4.337	4.309	4.337

Table 13
Compared $Ra = 10^7$ 3D air flow results

	$Ra = 10^7$		
Grid	Ref. [15] 27^3	Ref. [9] $33 \times 33 \times 29$	Present work 81^3
u_{max}	387.14		383.78
x	−0.377		−0.3777
y	0		0.37×10^{-10}
z	0.462		0.4663
v_{max}	80.28	58	83.40
x	−0.319		−0.3316
y	0.416		0.4083
z	0.403		0.3953
W_{max}	817.81	721	768.06
x	0.477		0.4775
y	0.459		0.4601
z	0.108		0.0323
$u_{mp,\ max}(0, 0, z)$			154.56
z			0.3716
$W_{mp,max}(x, 0, 0)$			686.93
x			−0.4755
N_{mp}	16.524		16.547
$N_{3D,\ W}$	16.317	16.2	16.342

Table 12
Compared $Ra = 10^6$ 3D air flow results

	$Ra = 10^6$				
Grid	Ref. [13] 62^3	Ref. [15] 27^3	Ref. [9] $33 \times 33 \times 29$	Ref. [14] 120^3	Present work 81^3
u_{max}		127.75			126.97
x		−0.307			−0.3057
y		0.306			0.2997
z		0.434			0.4365
v_{max}		25.15	23.5		25.56
x		0.448			0.4518
y		0.394			0.3983
z		0.410			0.4168
W_{max}		239.33	234.3		236.72
x		0.458			0.4604
y		0.430			0.4299
z		0.04			0.0265
$u_{mp,\ max}(0, 0, z)$	70.914			68.245	68.21
z	0.3557				0.3536
$W_{mp,\ max}(x, 0, 0)$	218.068			217.815	217.47
x	−0.4669				−0.4669
N_{mp}	9.012	8.876			8.877
$N_{3D,\ W}$	8.770	8.634	8.61	8.639	8.640

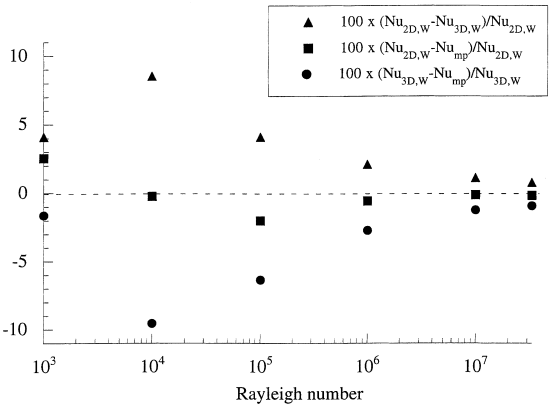

Fig. 3. The relative heat transfer rates as a function of the Rayleigh number.

Acknowledgements

The authors wish to thank the IDRIS (CNRS computing center) scientific committee for providing support through computing hours on the Cray-C98/C94, and the University Paris-Sud computing service for giving access to the Cray-YMP of CRI.

References

[1] A. Batoul, H. Khallouf, G. Labrosse, Une méthode de résolution directe (pseudo-spectrale) du problème de Stokes 2D/3D instationnaire, Application à la cavité entrainée carrée, C.R. Acad. Sci. Paris (1994), t.319, Serie 11, 1455–1461.

[2] G. Labrosse, E. Tric, H. Khallouf, B. Betrouni, A direct (pseudo-spectral) solver of the 2D/3D Stokes problem: transition to unsteadiness of natural-convection flow in a differentially heated cubical cavity, Num. Heat Transfer 31 (Part B) (1997) 261–276.

[3] W.H. Leong, K.G.T. Hollands, A.P. Brunger, On a physically-realizable benchmark problem in internal natural convection, Int. J. Heat Mass Transfer 41 (1998) 3817–3828.

[4] G. de Vahl Davis, I.P. Jones, Natural convection in a square cavity: a comparison exercise, Int. J. Num. Meth. Fluids 3 (1983) 227–248.

[5] G. de Vahl Davis, Natural convection of air in a square cavity: a bench-mark numerical solution, Int. J. Num. Meth. Fluids 3 (1983) 249–264.

[6] P. Le Quéré, Accurate solutions to the square thermally driven cavity at high Rayleigh number, Computers and Fluids 20 (1991) 29–41.

[7] P. Le Quéré, M. Behnia, From onset of unsteadiness to chaos in a differentially heated square cavity, J. Fluid Mech. 359 (1998) 81–107.

[8] G.D. Mallinson, G. de Vahl Davis, Three-dimensional natural convection in a box: a numerical study, J. Fluid Mech. 83 (1977) 1–31.

[9] P. Haldenwang, Résolution tridimensionnelle des équations de Navier–Stokes par méthodes spectrales Tchebycheff: application à la convection naturelle, Thése d'Etat, Université de Provence, 1984.

[10] P. Haldenwang, G. Labrosse, 2D and 3D spectral Chebyshev solutions for free convection at high Rayleigh number, in: Proc. 6th Int. Symposium on Finite Element Methods in Flow Problems, 1986, pp. 261–266.

[11] A.M. Lankhorst, J.C. Hoogendoorn, Three-dimensional numerical calculations of high Rayleigh number natural convective flows in enclosed cavities, in: Proc. 1988 Nat. Heat Transfer Conf. ASME HTD-96, vol. 3, 1988, pp. 463–470.

[12] T. Fusegi, J.M. Hyun, K. Kuwahara, B. Farouk, A numerical study of three-dimensional natural convection in a differentially heated cubical enclosure, Int. J. Heat Mass Transfer 34 (1991) 1543–1557.

[13] R.J.A. Janssen, R.A.W.M. Henkes, C.J. Hoogendoorn, Transition to time-periodicity of a natural-convection flow in a 3D differentially heated cavity, Int. J. Heat Mass Transfer 36 (1993) 2927–2940.

[14] A. Fikri, Simulation numérique 3D, en collocation Chebyshev, de phénoménes thermoconvectifs en centrifugation, Thése de l'Université Paris-Sud XI, Orsay, 1993.

[15] R.A.W.M. Henkes, P. Le Quéré, Three-dimensional transition of natural-convection flows, J. Fluid Mech. 319 (1996) 281–303.

[16] R.J.A. Janssen, R.A.W.M. Henkes, Instabilities in three-dimensional differentially-heated cavities with adiabatic horizontal walls, Phys. Fluids 8 (1996) 62–66.

[17] W.J. Hiller, S. Koch, T.A. Kowalewski, Three-dimensional structures in laminar natural convection in a cubic enclosure, Exp. Thermal and Fluid Sci. 2 (1989) 34–44.

[18] W.J. Hiller, S. Koch, T.A. Kowalewski, G. de Vahl Davis, M. Behnia, Experimental and numerical investigation of natural convection in a cube with two heated side walls, in: Proc. of IUTAM Symposium on Topological Fluid Mechanics, Cambridge, UK, Aug. 13–18, 1989, 1990, pp. 717–726.

[19] W.J. Hiller, S. Koch, T.A. Kowalewski, K. Range, M. Behnia, G. de Vahl Davis, Visualization of 3D natural convection–comparison with numerical results. In: Ed. Esp. da Revista Brasileira de Ciencias Mecanicas Sao Paulo, Proc. of 11th ABCM Mech. Eng. Conf. Sao Paulo (Brasil), Dec. 1991, pp. 21–24.

[20] T.A. Kowalewski, W.J. Hiller, G. de Vahl Davis, Computational and experimental visualisation in heat and mass transfer problems. In: Akiyama, Kleiber, Wolanski, (Eds.), Proc. of the First Japanese–Polish Joint Seminar in Advanced Computer Simulation, Tokyo, Nov. 8–9, 1993, University of Tokyo, 1994, pp. 60–69.

[21] A. Yarin, T.A. Kowalewski, W.J. Hiller, S. Koch, Distribution of particles suspended in 3D laminar convection flow, Physics of Fluids 8 (1996) 1130–1140.

[22] C. Canuto, M.Y. Hussaini, A. Quartcroni, T.A. Zang, Handbook of Spectral Method in Fluid Dynamics, Springer-Verlag, New York, 1988.

[23] G.E.M. Karniadakis, M. Israeli, S.A. Orszag, High-order splitting methods for the incompressible Navier–Stokes equations, J. Comput. Phys. 97 (1991) 414–443.
[24] E. Leriche, G. Labrosse, A direct Stokes solver without temporal splitting: its accuracy and stability properties, SIAM J. Scient. Comput., submitted.
[25] R.E. Lynch, J.R. Rice, H.T. Thomas, Direct solution of partial difference equations by tensor product methods, Numerische Mathematik 6 (1964) 185–199.
[26] P. Haldenwang, G. Labrosse, S. Abboudi, M. Deville, Chebyshev 3D spectral and 2D pseudospectral solvers for the Helmholtz equation, J. Comput. Phys. 56 (1984) 115–128.
[27] D. Gottlieb, S.A. Orszag, Numerical analysis of spectral methods: theory and applications, SIAM monograph no. 26, 1977.